From heterogenous morphogenetic fields to homogeneous regions as a step towards understanding complex tissue dynamics

Satoshi Yamashita*[1], Boris Guirao[2], and François Graner*[1]

[1]Laboratoire Matière et Systèmes Complexes (CNRS UMR7057), Université de Paris-Diderot, Paris, France

[2]Institut Curie, PSL Research University, CNRS UMR 3215, INSERM U934, F-75248 Paris Cedex 05, France

May 7, 2020

*Correspondence should be addressed to S.Y. (satoshiy83@gmail.com) and F.G. (francois.graner@univ-paris-diderot.fr)

1 Summary statement

Tissue morphogenesis is driven by multiple mechanisms. This study proposes a methodology to identify regions in the developing tissue, where each of the regions has distinctive cellular dynamics and deformation.

Abstract

Within developing tissues, cell proliferation, cell motility, and other cell behaviors vary spatially, and this variability gives a complexity to the morphogenesis. Recently, novel formalisms have been developed to quantify tissue deformation and underlying cellular processes. A major challenge for the study of morphogenesis now is to objectively define tissue sub-regions exhibiting different dynamics. Here we propose a method to automatically divide a tissue into regions where the local deformation rate is homogeneous. This was achieved by several approaches including image segmentation, clustering, and cellular Potts model simulation. We illustrate the use of the pipeline using a large dataset obtained during the metamorphosis of the *Drosophila* pupal notum. We also adapt it to determine regions where the time evolution of the local deformation rate is homogeneous. Finally, we generalize its use to find homogeneous regions for the cellular processes such as cell division, cell rearrangement, or cell size and shape changes. We also illustrate it on wing blade morphogenesis. This pipeline will contribute substantially to the analysis of complex tissue shaping and the biochemical and bio-mechanical regulations driving tissue morphogenesis.

2 Introduction

During tissue development, morphogenesis is accompanied by cellular processes such as cell division, cell rearrangement, apical constriction, and apoptosis. The cellular processes are coordinated together, yielding collective cell migration and local deformation of each tissue region, resulting in convergent extension or epithelial folding. Furthermore, the local deformations of different tissue regions are coordinated too, resulting in large scale tissue morphogenesis. Coordination between invaginating mesoderm and

covering ectoderm [Rauzi et al., 2015, Perez-Mockus et al., 2017], between invaginating midgut and elongating germ-band [Collinet et al., 2015, Lye et al., 2015, Dicko et al., 2017] of *Drosophila* embryo, between contracting wing hinge and expanding wing blade in *Drosophila* pupa [Etournay et al., 2015, Ray et al., 2015], or between invaginating neural plate and covering epidermal ectoderm of *Xenopus* embryo [Brodland et al., 2010], provide examples of how mechanical force generated in one region can drive large scale deformation in adjacent regions. In these cases, the regions which behave differently are easily distinguished by specific gene expressions.

However, many tissues were found to be heterogeneous but without obvious boundary between such regions, leaving analysis limited to arbitrary regions drawn as a grid parallel to tissue axes (Fig. 1A), or regions expressing already known differentiation maker genes. Measured tissue deformation rate showed a large heterogeneity (accompanied by a heterogeneity in cellular processes such as cell proliferation rate, cell division, cell rearrangement, change of cell shape), and smooth spatial variations across the tissue, in *Drosophila* notum in a developing pupa [Bosveld et al., 2012, Guirao et al., 2015] (Fig. 1B), *Drosophila* wing blade [Etournay et al., 2015], blastopore lip of *Xenopus* gastrula [Feroze et al., 2015], chick gastrula [Rozbicki et al., 2015, Firmino et al., 2016], mouse palatal epithelia [Economou et al., 2013], and mouse limb bud ectoderm [Lau et al., 2015]. Recent formalisms have enabled to measure and link quantitatively cellular processes with tissue deformation [Blanchard et al., 2009, Guirao et al., 2015, Etournay et al., 2015, Merkel et al., 2017]. However, cellular quantities also vary smoothly across the tissue. In addition, the causal relationship between cellular processes and tissue deformation is not always trivial, making it difficult to identify regions those actively drive morphogenesis and those passively deformed by adjacent regions.

To study the spatial regulation of morphogenesis at tissue scale, we developed a new multi-technique pipeline to divide a tissue into sub-regions based on quantitative measurements of static or dynamic properties of cells or tissues. Our tissue segmentation pipeline consists of three steps: a first fast tissue segmentation attempted several times with random seeding, then merging these multiple tissue segmentations into a single

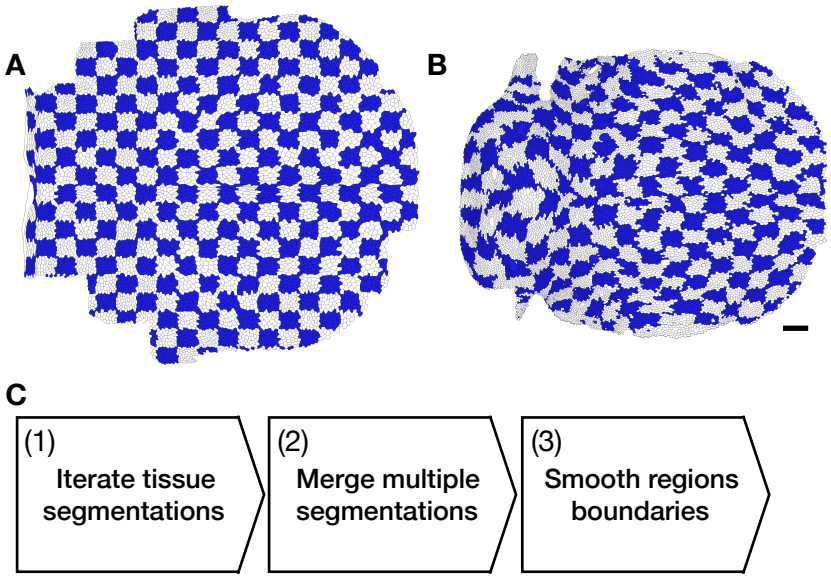

Fig. 1: Morphogenesis of *Drosophila* pupa notum and overview of tissue segmentation pipeline. (**A**, **B**) Heterogeneity of tissue morphogenesis. Here a *Drosophila* notum at 12 hr after pupa formation (APF), with arbitrary regions drawn from a grid (**A**), and at 32 hr APF, showing the heterogeneous deformation of previous regions using cell tracking (**B**). Cell patches are shown with blue and white check pattern. (**C**) Pipeline of the tissue segmentation. (1) Iteration of fast tissue segmentation with random seeding, using region growing algorithm. (2) Merging multiple tissue segmentations of step 1 into a single objective tissue segmentation, using label propagation algorithm on a consensus matrix. (3) Smoothing regions boundaries resulting of step 2, using cellular Potts model.

one, then smoothing the resulting regions boundaries (Fig. 1C). We apply it to the morphogenesis of *Drosophila* pupa dorsal thorax. The first application is to the tissue deformation rate integrated over the duration of a whole movie; the second application is to the time evolution of this tissue deformation rate; and the third application is to the time evolution of all cellular processes and their contribution to the local tissue deformation. Obtained sub-regions showed distinctive patterns of deformation and cellular processes with higher homogeneity than those along tissue axes. Interestingly, the tissue segmentations based on the local tissue deformation rate and on the cellular processes included some similar regions, suggesting that the cellular processes were regulated similarly inside the regions, therefore resulting in homogeneous tissue deformations inside those regions.

3 Results I : Development of automatic tissue segmentation algorithm

3.1 Image segmentation by region growing algorithm

Finding distinctive and homogeneous regions inside the heterogeneous tissue amounts to segmenting the geometrical space while keeping the points inside each of the regions as similar as possible to each other in the property space. Here, we call *property space* any morphogenesis quantification measured in the tissue, whereas *geometrical space* refers to the two-dimensional space of cell patch positions inside the tissue.

Given a set of objects, collecting similar objects to divide them into groups is generally a task of cluster analysis. However, the cell patches distribute in the property space and geometrical space. On the assumption that expression patterns of genes responsible for morphogenesis make connected regions, and to study physical interactions between the regions, we aimed at getting connected regions. The initial tissue segmentation first defines a metric of similarity between cells, and then a tissue is divided into regions containing similar cells. The image segmentation tool, called region growing [Adams and Bischof, 1994, Ma et al., 2010] (Fig. 2A), was inspired by a study segmenting mouse

heart based on cell polarity [Le Garrec et al., 2013].

To validate the algorithm, we first tested segmentation on a simple example, namely the change in cell patch areas from 12 to 32 hr APF (Fig. 2B). The overall change in cell patch areas defines the total tissue growth, while spatially heterogeneous changes in cell patch areas result in local deformation, changes in tissue region proportions, and overall tissue shape change. Technically speaking, the change in cell patch areas is a scalar field, defined as the trace of the tissue deformation rate tensor. The region growing succeeded in finding expanding regions in posterior, lateral posterior, and lateral parts and a shrinking region in anterior part.

However, the results varied dependent on the initial seeds. In contrast to a segmentation in histology or of immuno-stained image, where a true segmentation is well defined, the morphogenetic properties vary continuously with space, making it difficult to determine and validate the resultant segmentations. The silhouette, a measurement of region homogeneity (the silhouette of an object would be 1 if it was similar to all objects in the same cluster, and -1 if it was more similar to objects in other clusters), differed from one segmentation to the other (Fig. 2C). To assess the significancy of the homogeneity, we compared it with the average silhouette of randomly made control segmentations. Some of the region growing results had a low silhouette, even lower than that of half of the control segmentations (Fig. 2C), which means they were lacking any signification.

Among the various results because of the random initial seeding, we don't know which one should be compared with gene expression patterns or fed forward to a study of mechanical interactions between the regions. For practical applications, we need a single segmentation result for a given morphogenetic property.

3.2 Defining a single tissue segmentation using label propagation on a consensus matrix

To obtain a single tissue segmentation, we turned to consensus clusterings. In fact, since resultant segmentations of the region growing were dependent on randomly given initial values, we ran multiple trials and merged multiple segmentation results into a single

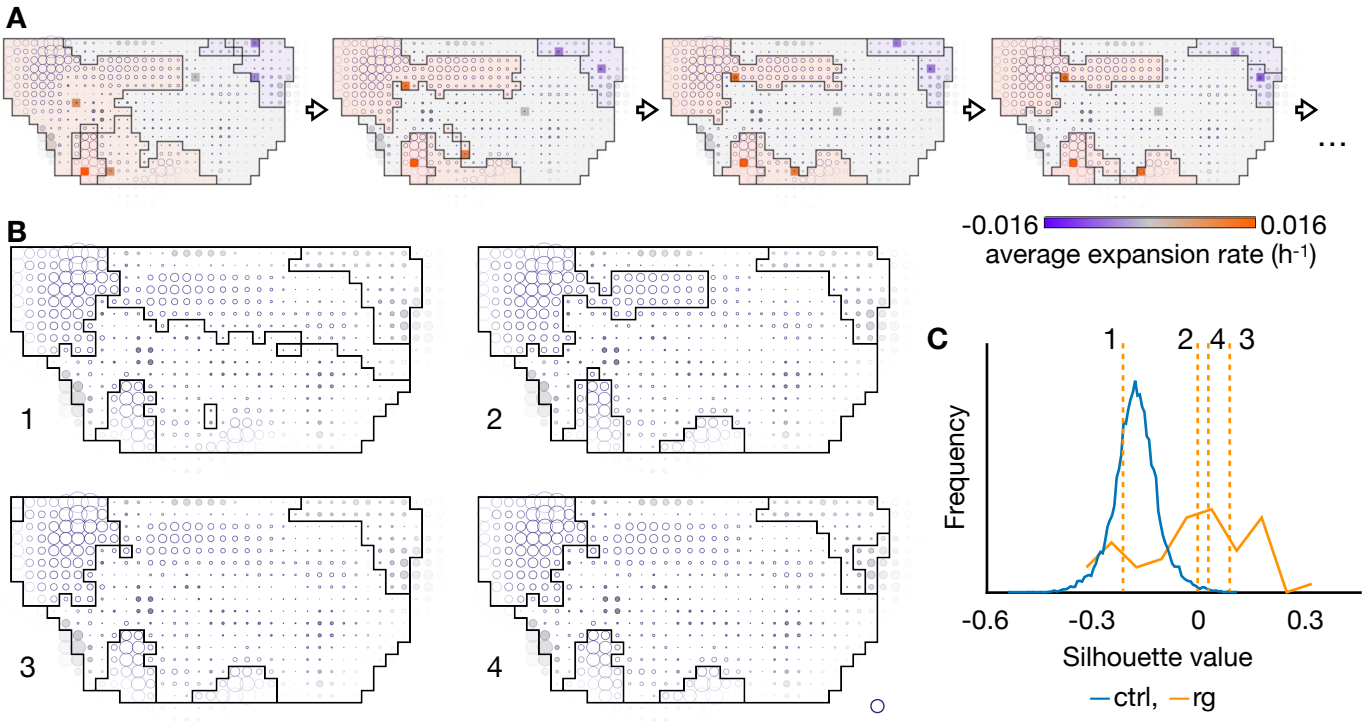

Fig. 2: Tissue segmentation by region growing algorithm. Cell patches expansion/contraction rates are represented by size of white/gray circles. (**A**) Process of region growing algorithm. Points of given number (6 in the shown example) are chosen randomly as initial seeds of regions, and the regions are expanded by collecting points similar to the seeds from their neighbors. Once the field is segmented, the seeds are updated to region centroids in the geometrical space and means in the property space, and the expansion of the regions are performed again from the new seeds. The seeds are shown with colored square, where the color represents an expansion rate of the regions. The regions are colored lighter for visibility. This update of the seeds and the regions are iterated until it reaches a convergence. (**B**) Four example results of region growing. (**C**) Histogram of silhouette value: blue for control segmentations, orange for region growing. Dotted vertical orange lines show silhouette values of the four examples shown in **B**.

one. Given multiple partitions, the consensus clustering returns the partition which is the most similar to all of the initial partitions. We tried several consensus clustering

algorithms, and found the *label propagation on a consensus matrix* [Lancichinetti and Fortunato, 2012, Raghavan et al., 2007] returning regions similar to the results of region growing.

The label propagation on a consensus matrix converted multiple tissue segmentations into a weighted graph where weight of an edge represented a frequency of segmentations in which incident vertices (points) belonged to the same region (Fig. 3A). Then labels on the vertices were propagated according to the weight so that the same label was assigned to points which were frequently included in the same region among the given multiple region growing segmentations.

The label propagation returned results similar to the region growing segmentations (Fig. 2B, 3B). Also, the label propagation results were more similar to each other than results of region growing, assessed with adjusted Rand indices (ARI), a measurement of similarity between two partitions (ARI of identical partitions would be 1). ARI were 0.50 ± 0.21 among the results of the region growing and 0.97 ± 0.02 among the results of the label propagation. They showed similar average silhouette values, similar to median of those of region growing results, but smaller than the highest value of those of region growing (Fig. 3C). The average silhouette of the label propagation result was higher than those of 99.95% of the randomly made control segmentations.

However, a consensus clustering algorithm ignores original properties of objects in principle and divides the objects only based on how they were divided among given partitions, and thus it might return disconnected regions and zigzag boundary between them. Some segmentations in Figure 3B also included disconnected regions as marked by gray color.

3.3 Smoothing of tissue segmentation results by cellular Potts model

To smooth the consensus regions boundaries, we employed cellular Potts model, which simulates dynamics of a cellular tissue by calculating energies of cells from their geometry, trying to decrease the total energy. In our application, the energy was lower when the region boundary was shorter and the homogeneity was higher (Fig. 4A). The boundary

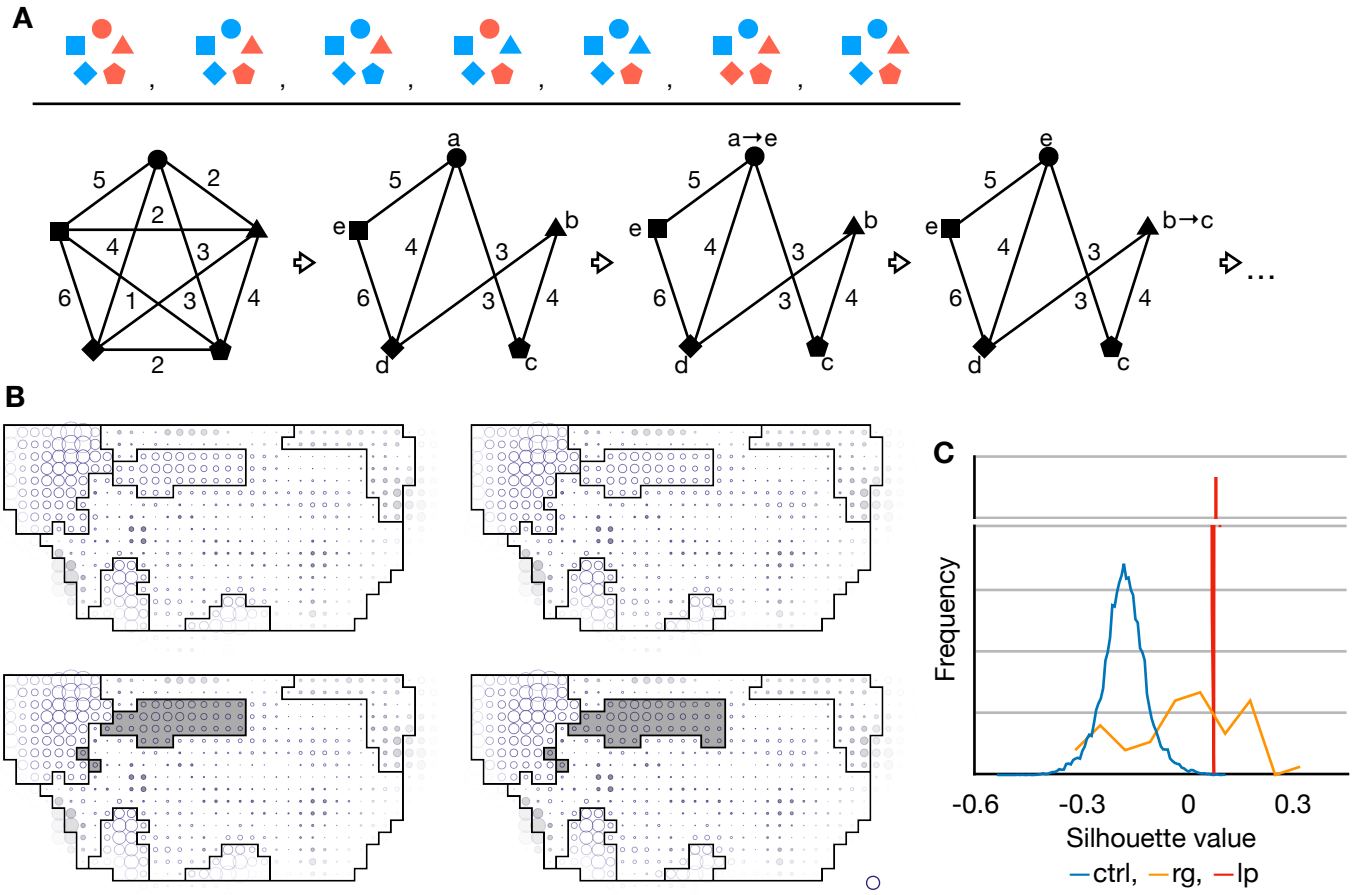

Fig. 3: Tissue segmentation by label propagation on a consensus matrix. (**A**) Process of label propagation algorithm. Multiple clusterings (upper) are converted to a consensus matrix, which gives weights to a complete graph on the objects being clustered (lower left). Edges with weights less than a given threshold are removed. All objects are initially assigned labels different to each other. And then, one by one in random order, each label is updated to the most frequent one weighted by edges incident to the object until it reaches a convergence. (**B**) Four example results of label propagation on the same consensus matrix. (**C**) Histogram of silhouette value: blue for control segmentations, orange for region growing, red for label propagation.

length and homogeneity were balanced so that all regions had enough smooth boundary, evaluated by a circularity [Bosveld et al., 2016], and was as homogeneous as possible.

It smoothed boundaries and removed disconnected cell patches (Fig. 4B, C) while keeping the average silhouette higher than those of random segmentations (Fig. 4D). Since the cellular Potts model simulation includes the Metropolis update, i.e., choosing a pixel randomly and updating the pixel by probability according to a change of the energy, resultant smoothed segmentations varied among different trials even with the same parameters and initial segmentation. Therefore we iterated the cellular Potts model smoothing 50 times and integrated its results by the label propagation algorithm again.

Now we have a pipeline of the region growing, the label propagation, and the cellular Potts model to divide a field of property (scalar, tensor, or any kind of value with metric) into regions. The resultant regions are homogeneous, where points in each region are more similar to each other than to points in other regions.

4 Results II : Tissue segmentation based on tissue morphogenesis

We now turn to property spaces better representing tissue morphogenesis. In Guirao et al. [2015], tissue deformation rate ($\mathbf{G}$) and underlying cellular processes, cell division ($\mathbf{D}$), cell rearrangement ($\mathbf{R}$), cell shape change ($\mathbf{S}$), and cell delamination ($\mathbf{A}$) were quantified into tensors. The tensors were obtained from change of the texture averaged over 20 hr from 12 hr APF to 32 hr APF or over 2 hr at each time point. By comparing the tensors, for example, one can check whether cell divisions and cell rearrangements elongated tissue in the same direction or attenuated each other. In the same way, by comparing the tensors of deformation rates with a unit tensor which has the same direction of elongation with tissue deformation rate, one can estimate an amplitude of the tissue deformation rate and how much the cellular processes contribute to the tissue deformation in both terms of contraction/expansion (isotropic deformation) and narrowing/elongation (anisotropic deformation) [Guirao et al., 2015]. They are scalar value and denoted by $\mathbf{G}_{/\!/}$ for the tissue deformation rate, $\mathbf{D}_{/\!/}$ for cell division, $\mathbf{R}_{/\!/}$ for cell

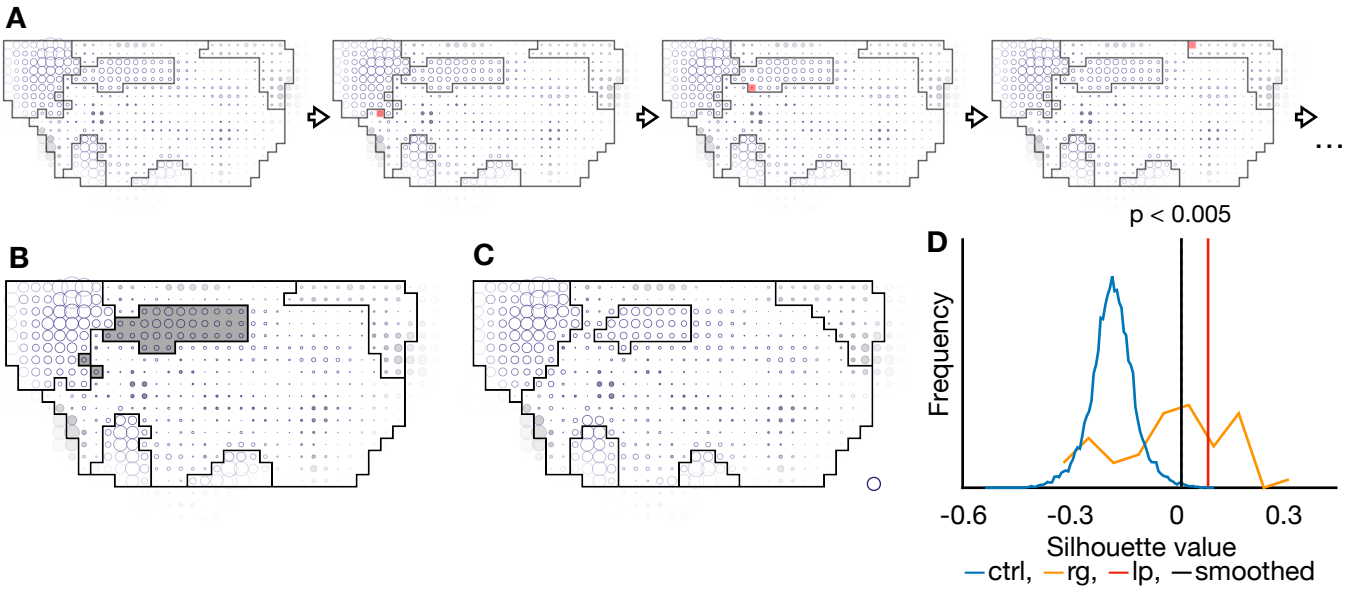

Fig. 4: Boundary smoothing by cellular Potts model. (**A**) Process of cellular Potts model. A pixel is randomly chosen and changes its belonging region if it decreases boundary length and/or increases homogeneity (marked by red). (**B**) Result of label propagation with a disconnected region shown by gray color. (**C**) Result of boundary smoothing by cellular Potts model. (**D**) Histogram of silhouette value: blue for control segmentations, orange for region growing, red vertical line for label propagation, and black vertical line for regions smoothed by cellular Potts model. Dotted blue line shows threshold for the highest 0.5% of the control segmentations.

rearrangement, $\mathbf{S}_{/\!/}$ for cell shape change, and $\mathbf{A}_{/\!/}$ for cell delamination (see appendix). For the sake of clarity, we call the tissue deformation rate and the cellular processes averaged over the whole 20 hr from 12 to 32 hr APF *time-average* tissue deformation rate and cellular processes.

The effective contributions averaged over the whole tissue showed dynamic time evolution (Fig. S1), with a large peak of cell division and cell shape change around 16 hr APF, second small wave of cell division around 22 hr APF, and gradual increase of cell shape change and cell rearrangement. The effective contributions also showed large variance across the tissue at each time point. Therefore we included the time evolution in the property space. Assume that there are two regions where one expands during 14-17 hr APF while another expands during 25-28 hr APF resulting in similar size changes, then the two regions cannot be distinguished by the time-average expansion rate. To distinguish them, we compared a property at each time point and summed up its difference through the whole time. When two cell patches always behaved similarly, then the difference at each time point is small and so the total difference is also small, whereas cell patches with deformations occurring in different timing are separated at each time point and thus the total difference get large. In contrast with time-average, we call the sum of difference at each time point *time-evolution*.

4.1 Tissue segmentations based on tissue deformation rate and cellular processes effective contributions

We first divided the tissue based on time-average and time-evolution of tissue deformation rate. The similarity was given by Euclidean distance of tensors (see methods for detail). The notum was divided into anterior-middle-posterior and medial-lateral regions by both of the time-average and time-evolution, while the middle regions were smaller and the middle lateral region extended medially in the segmentation based on time-evolution (Fig. 5A-D).

Next, we divided the tissue based on time-average and time-evolution of cellular processes. The amplitude of tissue deformation rate and cellular processes effective

contributions were combined in a vector, and their similarity was given by Euclidean distance of vector. In contrast to the segmentations based on the time-average and time-evolution of tissue deformation rate, the segmentations based on time-average and time-evolution of the cellular processes were dissimilar to each other (Fig. 5E-H). The segmentation based on time-evolution of cellular processes included a posterior region, a large anterior region, a neck-notum boundary region, lateral posterior region, a scutum-scutellum boundary region, and a lateral region (Fig. 5H).

4.2 Correspondence between segmentations based on cellular processes and tissue deformation rate

Both of the segmentations based on time-evolution of tissue deformation rate and cellular processes effective contributions included the large anterior region, the middle boundary region, the lateral posterior region, and the posterior region, although the anterior and posterior regions were divided into medial and lateral subregions in the segmentation based on the tissue deformation rate. Figure 6A-D show overlap between segmentation based on time-evolution of cellular processes (Fig. 5H) and the others (Fig. 5B, D, F) or a conventional large grid parallel to tissue axes. The middle lateral and posterior lateral regions in the segmentation based on time-evolution of tissue deformation rate and the middle scutum-scutellum boundary region and lateral posterior regions in the segmentation based on time-evolution of cellular processes overlapped each other (Fig. 6C). We also evaluated the overlap between the segmentations by ARI (Fig. 6E). Despite the difference between the anterior subregions, the segmentations based on time-evolution of tissue deformation rate and cellular processes overlapped each other more than the others.

4.3 Homogeneity of the obtained regions

Next, we evaluated the homogeneity of the obtained regions. The time-evolution of tissue deformation rate was similar among cells inside regions of the segmentations based on time-average and time-evolution of tissue deformation rate except the middle-lateral

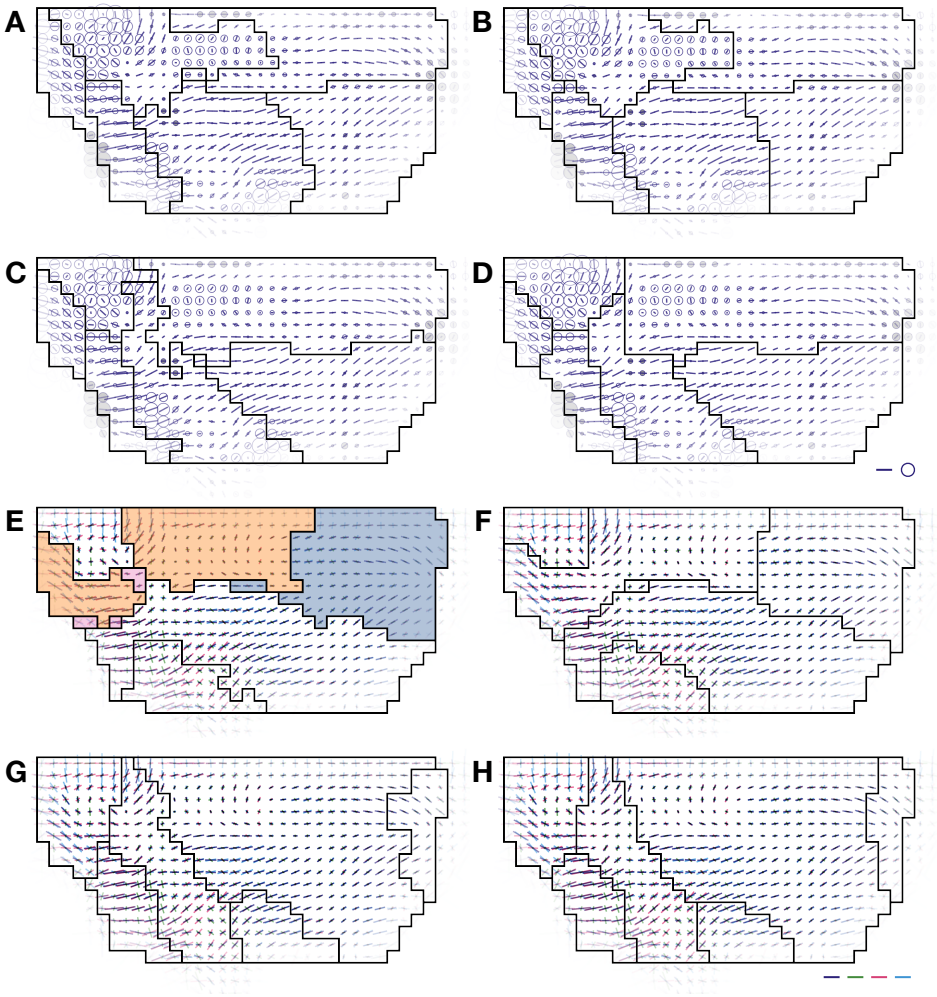

Fig. 5: Segmentations based on tissue deformation and underlying cellular processes. For each cell patch, direction of elongation is represented by a bar, and the effective contributions of cellular processes are indicated by relative directions of deformation rate between the tissue and each cellular process. For quantification and representation of tissue deformation rate and cellular processes, see methodology and Guirao et al. [2015]. (**A**-**H**) Segmentations based on time-average tissue deformation rate (**A**, **B**), time-evolution of deformation rate (**C**, **D**), time-average cellular processes effective contributions (**E**. **F**), and time-evolution of cellular processes (**G**, **H**). First column shows results of label propagation (**A**, **C**, **E**, **G**) and second column shows results of boundary smoothing (**B**, **D**, **F**, **H**).

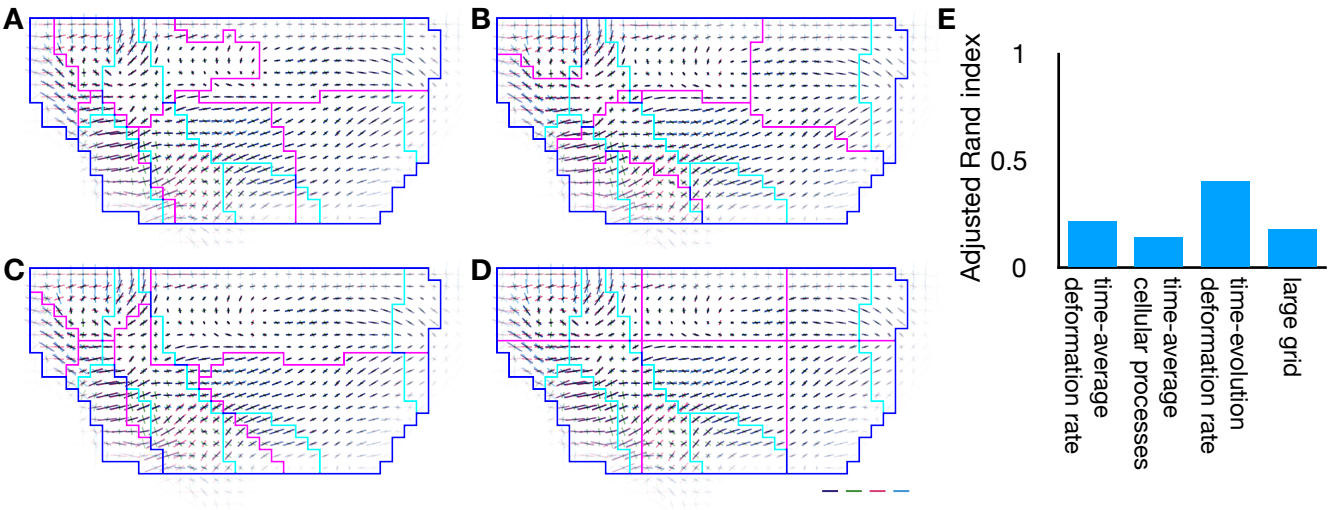

Fig. 6: Correspondence between segmentations based on cellular processes and deformation rate. (**A**-**D**) Overlays of segmentations, where segmentation based on time-evolution of deformation rate is shown by cyan line, while segmentations based on time-average deformation rate (**A**), time-average cellular processes (**B**), time-evolution of cellular processes (**C**), and large grid (**D**) are shown by magenta line. (**E**) Adjusted Rand indices of **A**-**D**.

region of the former (Fig. 7A, B). On the other hand, the large grid segmentation showed large heterogeneity in the posterior regions (Fig: 7C). The average silhouette value of the segmentation based on the time-evolution of deformation rate was higher than those of 99.5% of the control segmentations (average silhouette for label propagation: 0.0568, for smoothed regions: 0.0600, the maximum of the smallest 99.5% of controls average silhouettes: 0.0425) (Fig. 7D). The average silhouette of the segmentation based on time-averaged tissue deformation rate was also higher than 95% of the control segmentations (average silhouette for label propagation: 0.0336, for smoothed regions: 0.0260, the maximum of the smallest 95% of controls average silhouettes: -0.0098). On the other hand, that of the conventional grid segmentation was close to median of the control segmentations (average silhouette: -0.0694).

Also, the time-evolution of cellular processes was homogeneous inside the regions of

the segmentation based on time-evolution of cellular processes, but not in segmentation based on time-average of cellular processes nor in the grid (Fig. 7E-G). The average silhouette value of segmentation based on time-evolution was higher than 99.995% of control segmentations (average silhouette for label propagation: 0.147, for smoothed regions: 0.1448, the maximum of the smallest 99.995% of controls average silhouettes: 0.124), while that of segmentation based on time-average was smaller than 5% of control segmentations (average silhouette for label propagation: 0.0125, for smoothed regions: -0.0385, the maximum of the smallest 95% of controls average silhouettes: 0.0241) (Fig. 7H).

Our tissue segmentation is designed to divide a tissue into regions homogeneous in a given property space, and the homogeneity of either tissue deformation rate or cellular processes in the segmentations based on each property demonstrated that the pipeline worked fine (Fig. 7B, F). However, it does not assure the homogeneity of regions in a property space different from one based on which segmentation was performed. Figure S2 shows heat maps of silhouette values measured in different property spaces. Even though the homogeneity in the regions differed among the different property spaces, the segmentations based on time-evolution of tissue deformation rate and cellular processes showed higher homogeneity than the others also in the property spaces of deformation rates due to cell divisions, cell rearrangements, and cell shape changes.

We projected the regions divided based on the time-evolution of cellular processes onto the cells, and found that the anterior and posterior regions corresponded to scutum and scutellum, and the middle boundary and lateral posterior regions corresponded to the scutum-scutellum boundary (Fig. S4). This result demonstrates that the obtained regions corresponded to the anatomical features.

4.4 Cellular processes effective contributions inside the regions

Figure 8 shows plots of cellular processes effective contributions average in each region of the segmentation based on time-evolution of cellular processes. The second peak of cell division was observed only in the posterior regions and the scutum-scutellum bound-

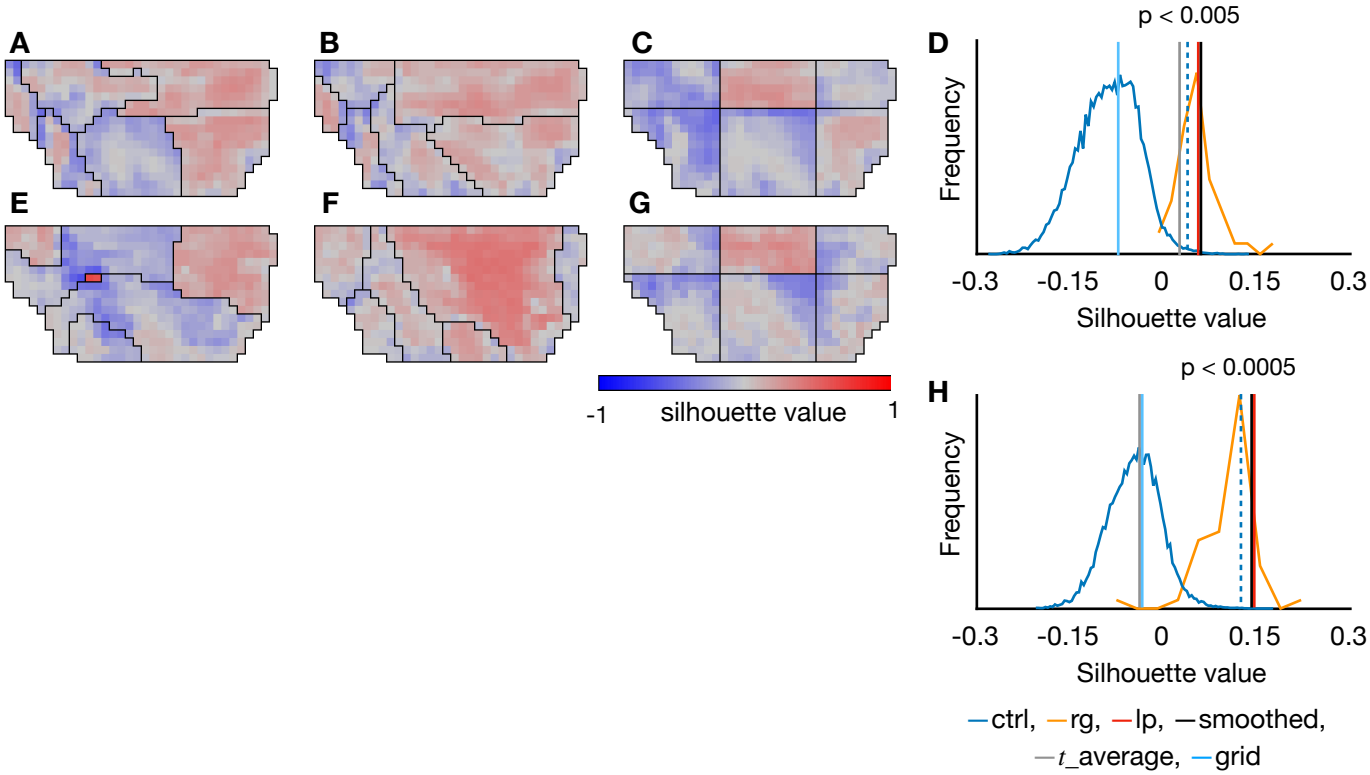

Fig. 7: Homogeneity in the obtained regions. (**A**-**C**) Heat map of silhouette value measured with time-evolution of tissue deformation rate in segmentations based on time-average deformation rate (**A**), time-evolution of deformation rate (**B**), and large grid (**C**). (**D**) Histogram of silhouette value: blue for control segmentations, orange for region growing. Red vertical lines show silhouette value of label propagation results. Black vertical lines show silhouette value of regions smoothed by cellular Potts model. Dotted blue lines show threshold for the highest 0.5% of the control segmentations. Gray and cyan vertical line shows silhouette value of segmentation based on time-averaged deformation rate and large grid. (**E**-**G**) Heat map of silhouette value measured with time-evolution of cellular processes effective contributions in segmentations based on time-average cellular processes (**E**), time-evolution of cellular processes (**F**), and large grid (**G**). (**H**) Histogram of silhouette value: blue for control segmentations, orange for region growing. Red vertical lines show silhouette value of label propagation results. Black vertical lines show silhouette value of regions smoothed by cellular Potts model. Dotted blue lines show threshold for the highest 0.05% of the control segmentations. Gray and cyan vertical line shows silhouette value of segmentation based on time-averaged cellular processes and large grid.

ary region, consistent with the preceding studies with maps of number of cell divisions [Bosveld et al., 2012, Guirao et al., 2015], while we also found the first peak of cell division small in the lateral posterior region. Plots of average cellular processes differed from each other also among regions in the segmentation based on tissue deformation rate but less distinctive in the large grid segmentation (Fig. S3). Distances between the plots in Figure 8 were 0.65 ± 0.16 and those for the segmentation based on tissue deformation rate were 0.63 ± 0.20, larger than those for large grid segmentation (0.44 ± 0.14). This result demonstrates that cellular processes in the obtained segmentations were more distinctive than those in the conventional grid.

4.5 Application to the morphogenesis of wing blade

To demonstrate the generality of our method to divide a tissue, we performed the same segmentation and analysis in the *Drosophila* pupa wing blade. During 15-32 hr APF, the wing blade is elongated in proximal-distal direction by a contracting wing hinge connected with the wing blade proximal side while its distal side is anchored to a cuticle via Dumpy [Etournay et al., 2015, Ray et al., 2015]. The wing hinge contraction also narrows it in the anterior-posterior direction and induces shear strain in wing blade proximal anterior and posterior regions (Fig. 9A, B). We performed the tissue segmentation for the wing blade based on time-evolution of tissue deformation rate (Fig. 9C) and cellular processes (Fig. 9D) dividing into four regions. In both cases, the wing blade was divided into anterior, middle, posterior, and distal regions. All regions showed positive silhouette values (Fig. 9E, F), and their averages were significantly higher than the average silhouette values of control segmentations (Fig. 9G, H). Plots of the cellular processes effective contributions also showed distinctive patterns between the regions, where the cell division showed small contribution in the anterior region, the cell rearrangements dominated the tissue deformation around 26 hr APF in the anterior and posterior regions, and the cell shape changes showed two peaks around 17 and 22 hr APF in the distal region (Fig. 9I). Projection of the four regions onto the cells showed a difference between the regions and interveins, whereas the posterior region roughly corresponded

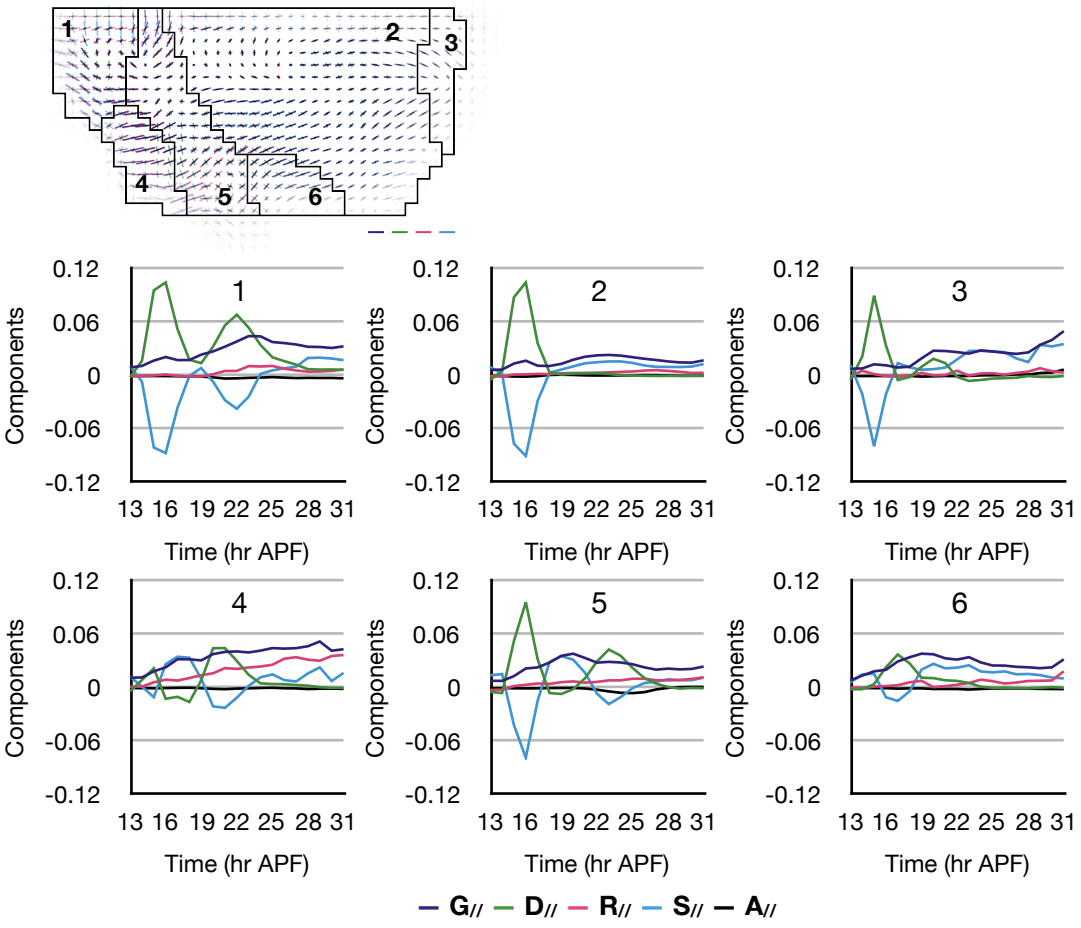

Fig. 8: Cellular processes effective contributions inside the regions. (**A**) Tissue segmentation based on time-evolution of deformation rate, where two anterior subregions were merged. (**B**) Plots of cellular processes effective contributions averaged in each region of 1-5 in **A**.

to the proximal posterior intervein and the boundary between the anterior and distal regions corresponded L3 vein (Fig. S5).

5 Discussion

This study demonstrates that the pipeline of the region growing, the label propagation on the consensus matrix, and the boundary smoothing by cellular Potts model could divide a deforming heterogeneous tissue into homogeneous regions based on the morphogenetic properties. Using this segmentation method, we divided the developing dorsal thorax and wing of *Drosophila* pupa, and found regions with distinctive tissue deformation rate and underlying cellular processes.

The tissue segmentation based on morphogenesis differs from conventional image segmentations, cell segmentations, and other tissue segmentations those are an automation of manual segmentation and can be corrected manually. First, the morphogenesis was quantified as multiple tensor fields with time evolution, and thus it is hard to visualize them in a 2D image for manual segmentation. Second, it is not easy to evaluate whether given a region actually corresponds to genetical/mechanical regulation of morphogenesis.

Fig. 9 *(following page)*: Segmentation of *Drosophila* wing blade into four regions. (**A**, **B**) Deformation of a wing blade from 15 hr (**A**) to 32 hr APF (**B**). Cell patches are shown with blue and white check pattern. (**C**, **D**) Segmentation based on time-evolution of tissue deformation rate (**C**) and its heat map of silhouette value (**D**). (**E**, **F**) Segmentation based on time-evolution of cellular processes (**E**) and its heat map of silhouette value (**F**). (**G**, **H**) Histogram of average silhouette value of control segmentations for the property spaces of tissue deformation rate (**G**) and cellular processes (**H**). Red vertical lines show average silhouette values of label propagation results. Black vertical lines show average silhouette values of smoothed regions. Dotted blue lines show threshold for the highest 0.05% (**G**) and 0.005% (**H**) of the control segmentations. (**I**) Plots of cellular processes effective contributions averaged in each region of 1-4 in **D**.

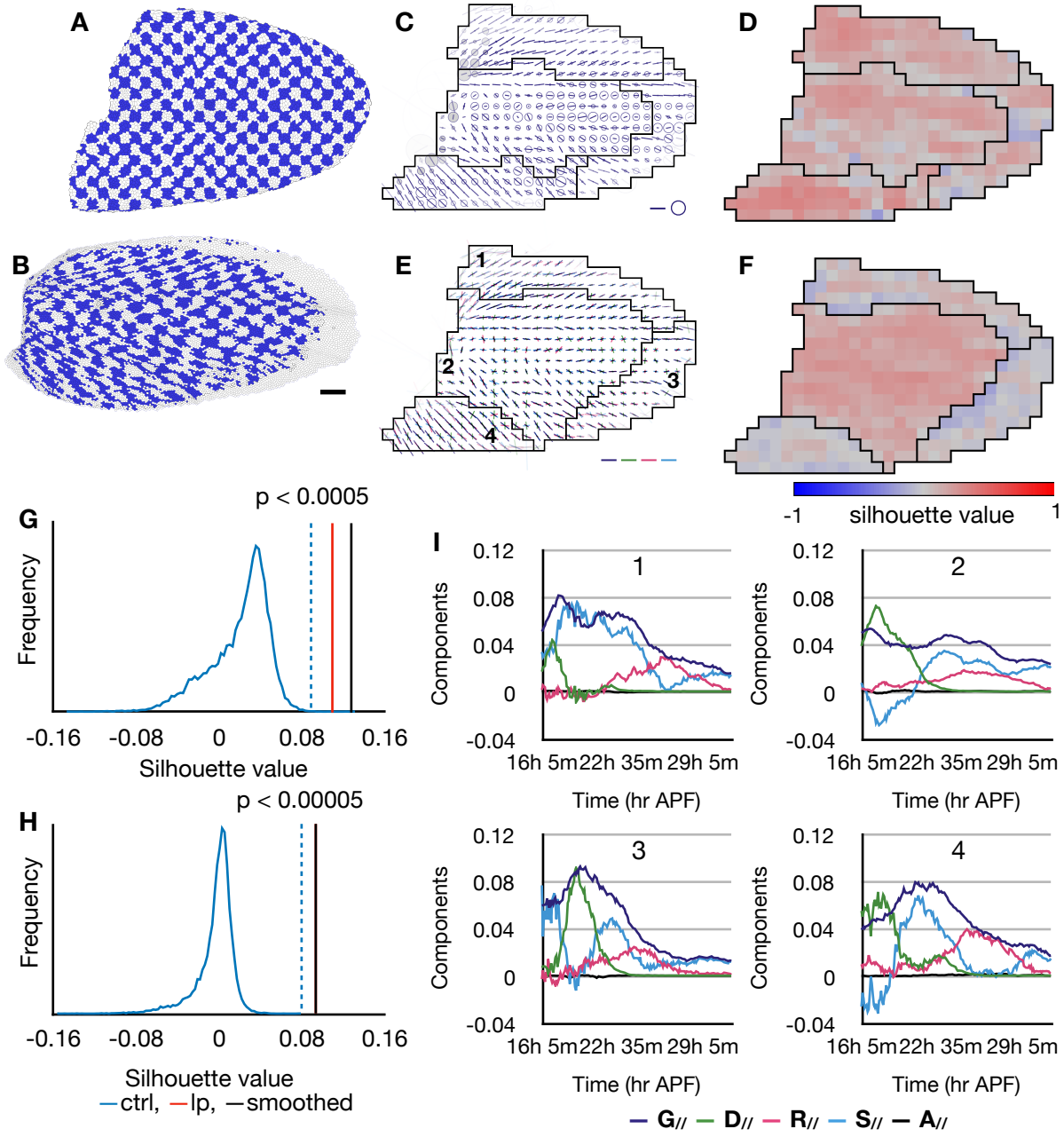

Therefore we looked for a method which divides a tissue based on any kind of quantity and returns regions with smooth boundaries. Region growing is a conventional and simple method of image segmentation, and requires a property space only to be metric. The varying results of the region growing were given to the label propagation and cellular Potts model to produce a single tissue segmentation, and the result was evaluated by homogeneity of the regions and smoothness of the boundary.

The notum segmentations based on time-evolution of tissue deformation rate and effective contributions cellular processes returned similar regions corresponding to the scutum, scutellum, and the boundary between them. By the tissue deformation rate, the scutum and scutellum regions were divided into medial and lateral subregions. Since the vector of effective contributions ignores the direction of deformation, the two subregions could be interpreted as regions of similar underlying cellular processes but deforming in different directions. On the other hand, the middle boundary region and the lateral region given by the cellular processes, both overlapped with the middle boundary region given by tissue deformation rate, could be interpreted as regions with different cellular processes but of similar tissue deformations. The wing blade was divided into anterior, middle, posterior, and distal regions based on both of the tissue deformation rate and cellular processes, but the regions did not matched the wing veins pattern.

Silhouette analysis showed that the segmentations based on time-evolution of deformation rate and cellular processes included regions homogeneous in various property spaces, whereas the conventional grid segmentation included heterogeneous regions.

In conclusion, we built a method to divide a tissue based on any kind of property space. This allows an application to a study of spatial regulation of various processes, where the property space should be chosen for the process of interest. For example, to study a spatial regulation of cell division orientation, the property space may be prepared from, instead of the local deformation rate and cellular processes, the tensor field of cell division and known regulating factors such as cell shape, localization of planar cell polarity proteins, and tension on cell-cell interface, and then resultant regions can be compared with genes expression patterns. Also, this method is not dependent on

how the morphogenesis was quantified, and one can include rotational movement by anti-symmetric strain rate tensors, or 3D deformation by using voxels instead of pixels.

6 Methods

6.1 Quantification tools

Morphogenesis data result from the quantification of local tissue deformation rate and underlying cellular processes as described in [Guirao et al., 2015]. The similarity between two tensors is quantified by the standard Euclidian metric. The homogeneity of a quantity within a given region, i.e. the similarity between measurements of this quantity within a region, is measured by silhouette, a standard tool of cluster analysis. For a measurement of similarity between tissue segmentations, we use the Rand index, which indicates how well two data clusterings agree.

6.1.1 Quantification of tissue deformation and cellular processes

Quantification of local tissue deformation and underlying cellular processes was performed in [Guirao et al., 2015]. Briefly, *Drosophila* nota expressing GFP-tagged E-cadherin were imaged. The notum movies were split in a grid (with patches about 20 μm width) at the first frame (Fig. 1C), 12 hr after pupa formation (APF). The local deformation rate and the cellular processes were measured in each cell patch through the development, as follows.

Epithelial cells contours were detected automatically using watershed algorithm, the cells were tracked, adjacencies between cells were listed, and relative positions of centers of adjacent cells were recorded. The tissue deformation rate, denoted by the symmetric tensor $\mathbf{G}$, was obtained from change of relative positions between neighbor cells over 20 hr from 12 hr APF to 32 hr APF, or over 2 hr at each time point when recording the time evolution. The tissue deformation rate $\mathbf{G}$ was then decomposed into cell shape change $\mathbf{S}$ and deformation accompanied by change of cell adjacency, which was further divided into cell division $\mathbf{D}$, cell rearrangement $\mathbf{R}$, and cell delamination $\mathbf{A}$, which are

symmetric tensors too.

In a collection of cells where the total deformation is driven completely by the four fundamental cellular processes, the tensors are in a balance equation,

$$\mathbf{G} = \mathbf{D} + \mathbf{R} + \mathbf{S} + \mathbf{A}. \tag{1}$$

The scalar product of two tensors $\mathbf{Q}$ and $\mathbf{Q}'$ in dimension d is defined as:

$$\mathbf{Q}.\mathbf{Q}' = \frac{1}{d}\mathrm{Tr}(\mathbf{Q}\mathbf{Q}'^{T}), \tag{2}$$

and the unitary tensor $\mathbf{u_G}$ that is aligned with $\mathbf{G}$ is given by

$$\mathbf{u_G} = \frac{\mathbf{G}}{(\mathbf{G}.\mathbf{G})^{1/2}}. \tag{3}$$

Since the scalar product (Eqn. 2) is a linear transformation, multiplying $\mathbf{u_G}$ by a tensor, the operation $.\mathbf{u_G} : \mathbf{Q} \rightarrow \mathbf{Q}_{/\!/}$, retains the balance between the tissue deformation rate and the cellular processes in Equation 1 while converting them to magnitudes:

$$\begin{aligned}
\mathbf{G}_{/\!/} =& \mathbf{G}.\mathbf{u_G} \\
=& (\mathbf{D} + \mathbf{R} + \mathbf{S} + \mathbf{A}).\mathbf{u_G} \\
=& \mathbf{D}.\mathbf{u_G} + \mathbf{R}.\mathbf{u_G} + \mathbf{S}.\mathbf{u_G} + \mathbf{A}.\mathbf{u_G} \\
=& \mathbf{D}_{/\!/} + \mathbf{R}_{/\!/} + \mathbf{S}_{/\!/} + \mathbf{A}_{/\!/}.
\end{aligned} \tag{4}$$

The scalar $\mathbf{G}_{/\!/}$ represents the local magnitude of tissue morphogenesis, and $\mathbf{D}_{/\!/}$, $\mathbf{R}_{/\!/}$, $\mathbf{S}_{/\!/}$, and $\mathbf{A}_{/\!/}$ represent the effective contributions of the cellular processes to the tissue morphogenesis. When a cellular process produces an anisotropic deformation in the same direction with that of tissue, e.g. cells divided in the same direction with tissue elongation, the scalar product between the them returns a positive value, while it returns negative value when a cellular process counteractes tissue deformation.

6.1.2 Metric

Similarity of morphogenesis between the cell patches was defined as follows.

For expansion/contraction of area (isotropic deformation), similarity was given by difference in expansion/contraction rates.

Similarity of anisotropic deformation was given by a distance between two tensors **Q** and **Q'**,

$$d(\mathbf{Q}, \mathbf{Q'}) = \left\{ \left(\frac{\mathbf{Q}_{xx} - \mathbf{Q}_{yy}}{2} - \frac{\mathbf{Q'}_{xx} - \mathbf{Q'}_{yy}}{2} \right)^2 + (\mathbf{Q}_{xy} - \mathbf{Q'}_{xy})^2 \right\}^{1/2}. \tag{5}$$

For tensors with time-evolution $\mathbf{Q}(t)$ and $\mathbf{Q'}(t)$, distance was given by a sum of the distance at each time point,

$$|\mathbf{Q} - \mathbf{Q'}| = \int d(\mathbf{Q}(t), \mathbf{Q'}(t))dt, \tag{6}$$

as an analogy to distance between functions.

For the composition of cellular processes, the tensors of cellular processes were converted to effective contributions and combined into a vector ($\mathbf{G}_{/\!/}, \mathbf{D}_{/\!/}$, $\mathbf{R}_{/\!/}$, $\mathbf{S}_{/\!/}$, $\mathbf{A}_{/\!/}$). A distance between two vectors was given by Euclidean distance, the square root of the sum of the square of the differences between corresponding elements, and a distance between vectors with time-evolution $v(t)$ and $v'(t)$ was given by a sum of the distance at each time point,

$$|v - v'| = \int ||v(t) - v'(t)||dt. \tag{7}$$

6.1.3 Silhouette and bootstrap

Silhouette quantifies clustering results, indicating how well an object resembles other objects inside its own cluster [Rousseeuw, 1987]. Assume that n objects $\{p_1, p_2, \ldots, p_n\}$ are partitioned into k clusters $\{C_1, C_2, \ldots, C_k\}$. For an object $p_i \in C_I$, we can compute average distance $a(p_i)$ from p_i to all other objects in C_I. For $J \neq I$, we can also compute average distance $d(p_i, C_J)$ from p_i to all objects in C_J, and can select the smallest of those, denoted by $b(p_i) = \min_{J \neq I} d(p_i, C_J)$. The silhouette value $s(p_i)$ is obtained by combining $a(p_i)$ and $b(p_i)$ as follow:

$$s(p_i) = \frac{b(p_i) - a(p_i)}{\max\{a(p_i), b(p_i)\}}. \tag{8}$$

By this definition, $-1 \leq s(p) \leq 1$, where $s(p)$ large and close to 1 indicates that p is similar to other objects in the same cluster, while negative $s(p)$ indicates that there is another cluster whose objects are more similar to p than objects in the cluster containing p.

We took the average silhouette value over all points (cell patches) as a measurement of homogeneity of a given segmentation. For significance test, tissue was segmented randomly 20,000 times into a given number, and we got thresholds above which the highest 5%, 0.5%, or 0.005% of the average silhouettes were found. The average silhouette of given regions were compared to those of the control segmentations with the same number of regions.

6.1.4 Adjusted Rand index

For a measurement of similarity between tissue segmentations, we use the Rand index, which indicates how well two data clusterings agree ; its value is 0 if the clusterings entirely disagree and 1 if they entirely agree. Its corrected-for-chance version is a more meaningful quantity, called the adjusted Rand index (ARI): it is the Rand index minus its value expected for the random case, and its value can be negative.

We compute the adjusted Rand index with the permutation model [Hubert and Arabie, 1985]. Given two clusterings $A = \{A_1, \ldots, A_k\}$ and $B = \{B_1, \ldots, B_m\}$ of N elements, the contingency table $\tau = (n_{ij})_{k \times m}$ is made where $n_{ij} = |A_i \cap B_j|$. The Rand index between A and B, $\mathrm{RI}(A, B)$ is given by the function

$$\mathrm{RI}(A,B) = \frac{2\sum_{ij}\binom{n_{ij}}{2} - \sum_i \binom{a_i}{2} - \sum_j \binom{b_j}{2} + \binom{N}{2}}{\binom{N}{2}}, \tag{9}$$

where $a_i = \sum_j n_{ij}$ and $b_j = \sum_i n_{ij}$, and an expected Rand index $\mathbb{E}[\mathrm{RI}(A, B)]$ is given

by the function

$$\mathbb{E}[\mathrm{RI}(A,B)] = \frac{\sum_i \binom{a_i}{2} \sum_j \binom{b_j}{2}}{\binom{N}{2} \binom{N}{2}} + \left(1 - \frac{\sum_i \binom{a_i}{2}}{\binom{N}{2}}\right)\left(1 - \frac{\sum_j \binom{b_j}{2}}{\binom{N}{2}}\right). \quad (10)$$

The adjusted Rand index $\mathrm{ARI}(A,B)$ is given by the function

$$\mathrm{ARI}(A,B) = \frac{\mathrm{RI}(A,B) - \mathbb{E}[\mathrm{RI}(A,B)]}{1 - \mathbb{E}[\mathrm{RI}(A,B)]}. \quad (11)$$

6.2 Tissue segmentation pipeline

The pipeline was implemented by custom Matlab scripts, in three steps (Fig. 1C). The Matlab scripts are available at GitHub (https://doi.org/10.5281/zenodo.3626111).

6.2.1 Region growing tissue segmentation

The initial tissue segmentation first defines a metric of similarity between cells, and then a tissue is divided into regions containing similar cells. This approach was inspired by a study segmenting mouse heart based on cell polarity [Le Garrec et al., 2013]. On the assumption that expression patterns of genes responsible for morphogenesis make connected regions, and to study physical interactions between the regions, we aimed at getting connected regions.

The algorithm *Region growing* [Adams and Bischof, 1994, Ma et al., 2010] is an image segmentation method using a process similar to k-means clustering, starting from randomly given seeds (corresponding to "means" in k-means clustering), segmenting an image with the seeds followed by update of the seeds within the regions, and iterating this process until convergence (Fig. 2A). The tissue segmentation is done by growing regions from the seeds collecting pixels adjacent to the growing regions, and so the resultant regions are connected.

Initial seeds were randomly chosen from data, and regions were expanded by adding a pixel (cell patch) adjacent to a region and the most similar to the seed of the region

in the property space one by one until all pixels were assigned to one of the regions. The seeds were updated to pixels the closest to centroids of the regions, averages of the regions in the property space were given as property of the seeds, and then regions were expanded again from the seeds. These region expansions and seeds updates were iterated until convergence was reached.

6.2.2 Label propagation on a consensus matrix

To merge multiple segmentation results into a single one independent on the metric, we use label propagation algorithm on a consensus matrix, which takes multiple partitions and returns a consensus partition which is the most similar to all partitions [Lancichinetti and Fortunato, 2012, Raghavan et al., 2007].

For a division of n points, independent 50 trials of region growing were converted to a consensus matrix, whose entry at i-th row and j-th column indicates a frequency of partitions in which i-th point and j-th point were in the same cluster. The entries lower than a given threshold were set to 0. The label propagation started by assigning to each point a different label. Then the label of randomly chosen i-th point was updated to one that was the most weighted by the consensus matrix, where ij element gave the weight to a label of j-th point. The label update was iterated until convergence. The threshold for the consensus matrix was scanned between 20-80% so that a resultant partition contained the same number of regions as the initial partitions.

6.2.3 Cellular Potts model

To smooth the consensus region boundaries while preserving region area and homogeneity, we use the cellular Potts model, in which a cellular structure is numerically simulated in a square lattice, where each cell is a set of pixels. An energy of system depends on the shape of cells, and the pattern is updated in an iteration to decrease the energy, with some fluctuation allowance [Graner and Glazier, 1992]. In the simplest and common two-dimensional form, the energy $\mathcal{H}$ arises from total perimeter length P (with line energy J) and constraint on each region area A (with compressibility λ); decreasing

it results in smoother region with preserved area A_0, removing small protrusions and disconnected regions. In this study, we also included the silhouette s to account for the region homogeneity, with a weight coefficient h: $\mathcal{H} = \sum_{\text{regions}} \left[JP + \lambda(A - A_0)^2 - hs \right]$. The coefficients J, λ, and h were adjusted manually on a case by case basis.

When updating the label for a randomly selected pixel a, a target label was randomly selected from neighbors of a, and then change of the Hamiltonian was calculated and updated label of a to the target label with probability $min(1, e^{-\Delta\mathcal{H}/T})$, where $\Delta\mathcal{H}$ denotes change of $\mathcal{H}$ by the change of label of a, and T is the fluctuation allowance. In the simulations, the updates of labels were iterated 50 times. For resultant regions, a circularity C was calculated, where it was defined as $C = 4\pi \times \text{area}/\text{perimeter}^2$ in Bosveld et al. [2016]. The parameters J, λ, h, and T were screened for resultant regions with the highest homogeneity and circularity larger than 0.45. With the screened parameters, the boundary smoothing was iterated for 50 times, and the results were integrated again by the label propagation on a consensus matrix algorithm.

7 Acknowledgement

The authors thank Floris Bosveld for imaging, Stéphane U. Rigaud for cell segmentation and tracking, Yohanns Bellaïche for useful advises, and all team members for insightful discussions.

8 Competing interests

The authors declare no competing nor financial interests.

9 Author contributions

Quantification of morphogenesis: B.G.; Methodology: S.Y., F.G.; Definition of metric: S.Y., F.G.; Programming and implementation: S.Y.; Writing and editing: S.Y., F.G.; Supervision: F.G.

10 Funding

This research was supported by grants to S.Y. from Uehara Memorial Foundation (201630059), Japan Society for the Promotion of Science (201860572).

References

R. Adams and L. Bischof. Seeded region growing. *IEEE Trans Pattern Anal Mach Intell*, 16:641–647, Jun 1994.

G. B. Blanchard, A. J. Kabla, N. L. Schultz, L. C. Butler, B. Sanson, N. Gorfinkiel, L. Mahadevan, and R. J. Adams. Tissue tectonics: morphogenetic strain rates, cell shape change and intercalation. *Nat Methods*, 6:458–464, 2009.

F. Bosveld, I. Bonnet, B. Guirao, S. Tlili, Z. Wang, A. Petitalot, R. Marchand, P.-L. Bardet, P. Marcq, F. Graner, and Y. Bellaïche. Mechanical control of morphogenesis by fat/dachsous/four-jointed planar cell polarity pathway. *Science*, 336:724–727, 2012.

F. Bosveld, B. Guirao, Z. Wang, M. Riviere, I. Bonnet, F. Graner, and Y. Bellaïche. Modulation of junction tension by tumor suppressors and proto-oncogenes regulates cell-cell contacts. *Development*, 143(4):623–634, Feb 2016.

G. W. Brodland, X. Chen, P. Lee, and M. Marsden. From genes to neural tube defects (ntds): insights from multiscale computational modeling. *HFSP J*, 4:142–152, 2010.

C. Collinet, M. Rauzi, P.-F. Lenne, and T. Lecuit. Local and tissue-scale forces drive oriented junction growth during tissue extension. *Nat Cell Biol*, 17:1247–1258, 2015.

M. Dicko, P. Saramito, G. B. Blanchard, C. M. Lye, B. Sanson, and J. Etienne. Geometry can provide long-range mechanical guidance for embryogenesis. *PLoS Comput. Biol.*, 13(3):e1005443, Mar 2017.

A. D. Economou, L. J. Brock, M. T. Cobourne, and J. B. Green. Whole population

494 cell analysis of a landmark-rich mammalian epithelium reveals multiple elongation
495 mechanisms. *Development*, 140(23):4740–4750, Dec 2013.

496 R. Etournay, M. Popović, M. Merkel, A. Nandi, C. Blasse, B. Aigouy, H. Brandl, G. My-
497 ers, G. Salbreux, F. Julicher, and S. Eaton. Interplay of cell dynamics and epithelial
498 tension during morphogenesis of the Drosophila pupal wing. *Elife*, 4:e07090, Jun 2015.

499 R. Feroze, J. H. Shawky, M. von Dassow, and L. A. Davidson. Mechanics of blastopore
500 closure during amphibian gastrulation. *Dev. Biol.*, 398(1):57–67, Feb 2015.

501 J. Firmino, D. Rocancourt, M. Saadaoui, C. Moreau, and J. Gros. Cell Division Drives
502 Epithelial Cell Rearrangements during Gastrulation in Chick. *Dev. Cell*, 36(3):249–
503 261, Feb 2016.

504 F. Graner and J. A. Glazier. Simulation of biological cell sorting using a two-dimensional
505 extended Potts model. *Phys. Rev. Lett.*, 69(13):2013–2016, Sep 1992.

506 B. Guirao, S. U. Rigaud, F. Bosveld, A. Bailles, J. Lopez-Gay, S. Ishihara, K. Sugimura,
507 F. Graner, and Y. Bellaïche. Unified quantitative characterization of epithelial tissue
508 development. *Elife*, 4:e08519, Dec 2015.

509 L. Hubert and P. Arabie. Comparing partitions. *Journal of Classification*, 2:193–218,
510 1985.

511 A. Lancichinetti and S. Fortunato. Consensus clustering in complex networks. *Sci Rep*,
512 2:336, 2012.

513 K. Lau, H. Tao, H. Liu, J. Wen, K. Sturgeon, N. Sorfazlian, S. Lazic, J. T. A. Burrows,
514 M. D. Wong, D. Li, S. Deimling, B. Ciruna, I. Scott, C. Simmons, R. M. Henkelman,
515 T. Williams, A.-K. Hadjantonakis, R. Fernandez-Gonzalez, Y. Sun, and S. Hopyan.
516 Anisotropic stress orients remodelling of mammalian limb bud ectoderm. *Nat Cell*
517 *Biol*, 17:569–579, 2015.

J. F. Le Garrec, C. V. Ragni, S. Pop, A. Dufour, J. C. Olivo-Marin, M. E. Buckingham, and S. M. Meilhac. Quantitative analysis of polarity in 3D reveals local cell coordination in the embryonic mouse heart. *Development*, 140(2):395–404, Jan 2013.

C. M. Lye, G. B. Blanchard, H. W. Naylor, L. Muresan, J. Huisken, R. J. Adams, and B. Sanson. Mechanical Coupling between Endoderm Invagination and Axis Extension in Drosophila. *PLoS Biol.*, 13(11):e1002292, 2015.

Z. Ma, J. M. Tavares, R. N. Jorge, and T. Mascarenhas. A review of algorithms for medical image segmentation and their applications to the female pelvic cavity. *Comput Methods Biomech Biomed Engin*, 13(2):235–246, 2010.

M. Merkel, R. Etournay, M. Popović, G. Salbreux, S. Eaton, and F. Julicher. Triangles bridge the scales: Quantifying cellular contributions to tissue deformation. *Phys Rev E*, 95(3-1):032401, Mar 2017.

G. Perez-Mockus, K. Mazouni, V. Roca, G. Corradi, V. Conte, and F. Schweisguth. Spatial regulation of contractility by Neuralized and Bearded during furrow invagination in Drosophila. *Nat Commun*, 8(1):1594, Nov 2017.

U. N. Raghavan, R. Albert, and S. Kumara. Near linear time algorithm to detect community structures in large-scale networks. *Phys Rev E Stat Nonlin Soft Matter Phys*, 76(3 Pt 2):036106, Sep 2007.

M. Rauzi, U. Krzic, T. E. Saunders, M. Krajnc, P. Ziherl, L. Hufnagel, and M. Leptin. Embryo-scale tissue mechanics during Drosophila gastrulation movements. *Nat Commun*, 6:8677, 2015.

R. P. Ray, A. Matamoro-Vidal, P. S. Ribeiro, N. Tapon, D. Houle, I. Salazar-Ciudad, and B. J. Thompson. Patterned Anchorage to the Apical Extracellular Matrix Defines Tissue Shape in the Developing Appendages of Drosophila. *Dev. Cell*, 34(3):310–322, Aug 2015.

543 P. Rousseeuw. Silhouettes: a graphical aid to the interpretation and validation of cluster
544 analysis. *Computational and Applied Mathematics*, 20:53–65, 1987.

545 E. Rozbicki, M. Chuai, A. I. Karjalainen, F. Song, H. M. Sang, R. Martin, H.-J. Knölker,
546 M. P. MacDonald, and C. J. Weijer. Myosin-ii-mediated cell shape changes and cell
547 intercalation contribute to primitive streak formation. *Nat Cell Biol*, 17:397–408, 2015.

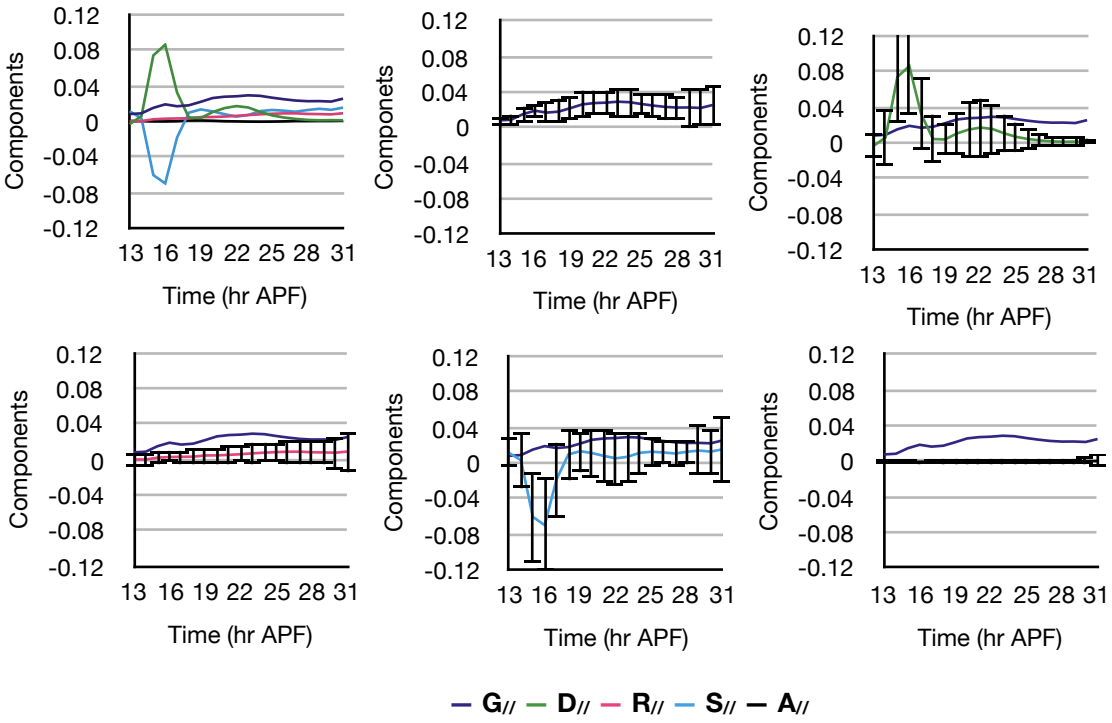

Fig. S1: Variance of effective contribution of cellular processes at each time point. Plots show time evolution of effective contribution of cellular processes in the *Drosophila* notum and standard deviation of them.

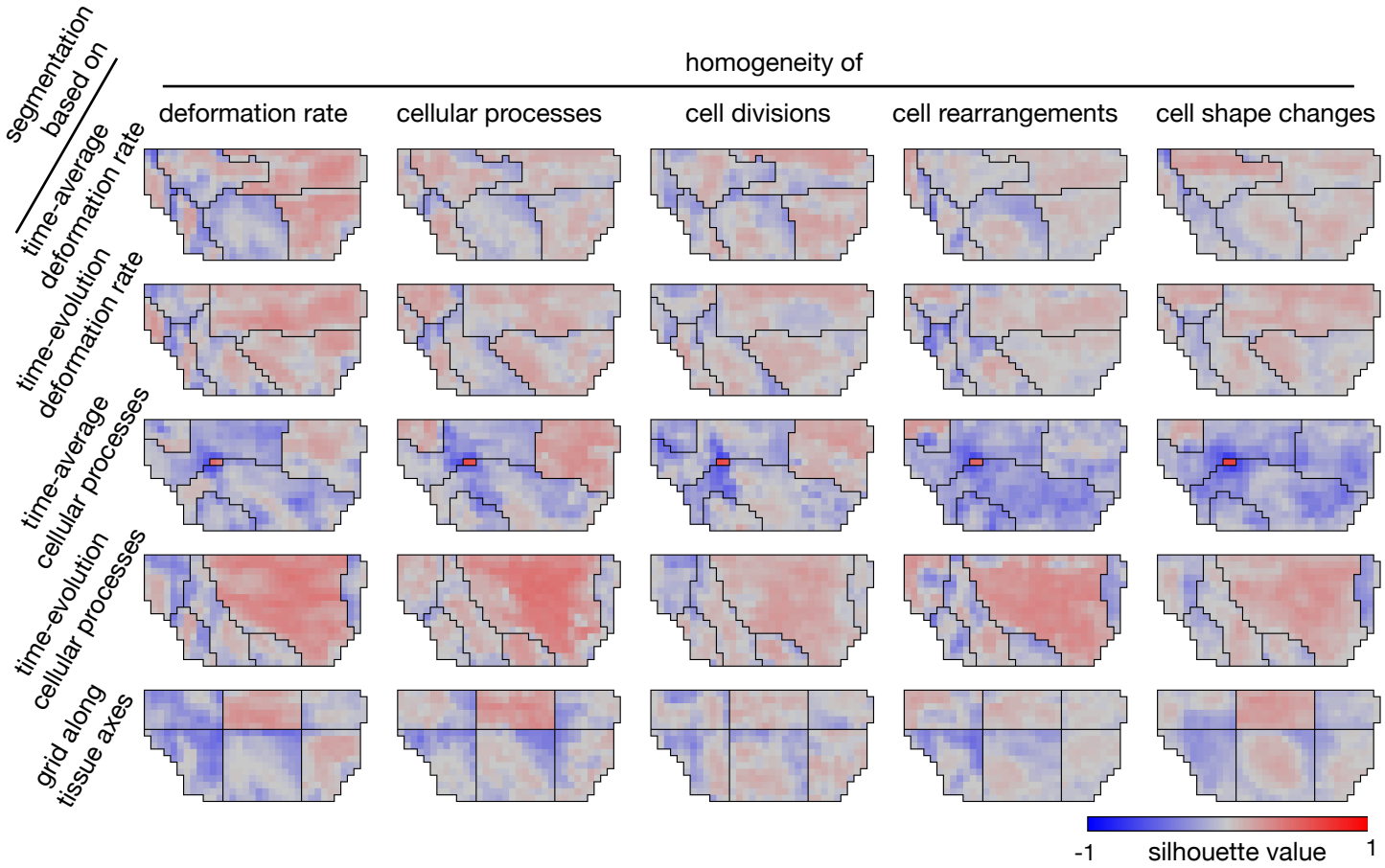

Fig. S2: Heat maps of silhouette value. First row: segmentation based on time-average tissue deformation rate. Second row: segmentation based on time-evolution of deformation rate. Third row: segmentation based on time-average cellular processes effective contributions. Fourth row: segmentation based on time-evolution of cellular processes. Fifth row: conventional segmentation of large grid parallel to tissue axes. First column: silhouette values measured in the property space of time-evolution of deformation rate. Second column: silhouette values measured by time-evolution of cellular processes. Third column: silhouette values measured by time-evolution of cell divisions. Fourth column: silhouette values measured by time-evolution of cell rearrangements. Fifth column: silhouette values measured by time-evolution of cell shape changes.

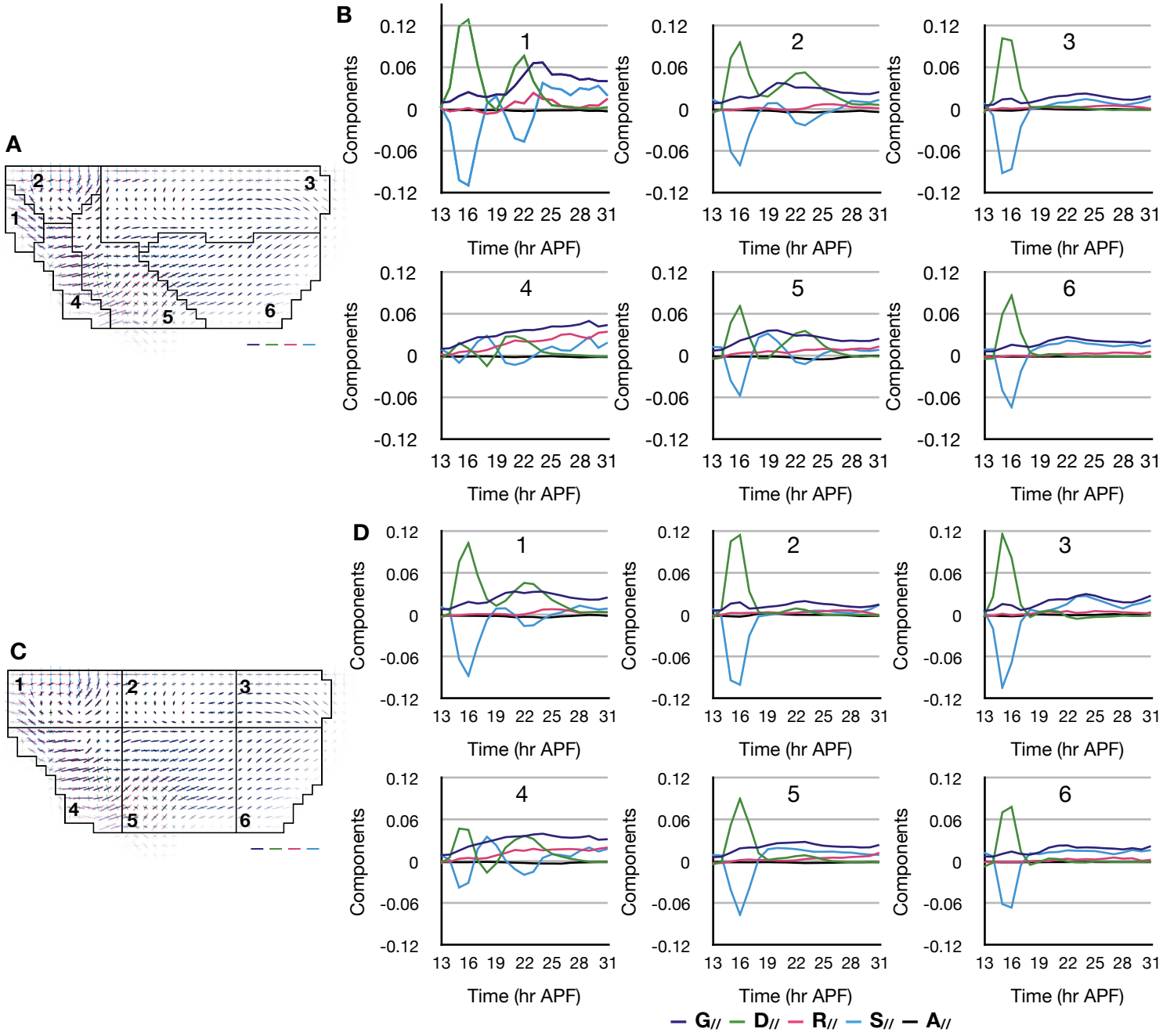

Fig. S3: Plots of cellular processes in the segmentations based on time evolution of tissue deformation rate and the conventional large grid. (**A**, **B**) The tissue segmentation based on time-evolution of tissue deformation rate (**A**) and plots of cellular processes effective contributions averaged in each region (**B**). The numbers indicate the regions. (**C**, **D**) The large grid (**C**) and plots of cellular processes in each region (**D**). Scale bars in **A** and **C** indicate deformation rate 0.02 h^{-1} with colors for tissue and cellular processes.

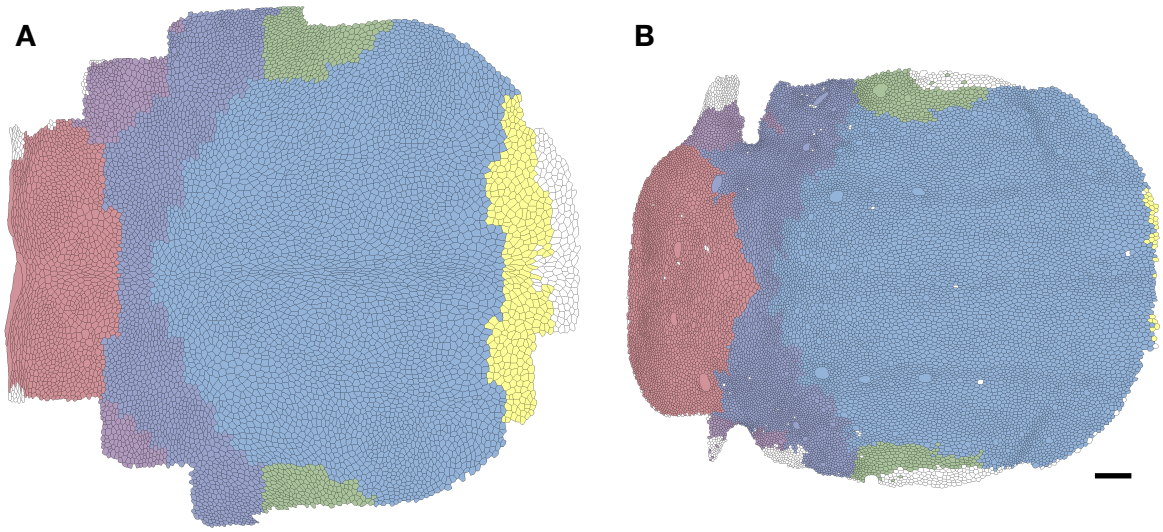

Fig. S4: Projection of the segmentation onto the notum cells. The segmentations based on time evolution of cellular processes were projected. (**A**, **B**) The segmentation was projected onto the notum cells at 12 hr (**A**) and 32 hr APF (**B**), where regions were indicated by colors. The regions corresponded to scutum (pale blue and green), scutellum (red), and boundary between them (dark blue and purple). Scale bars indicate 50 μm.

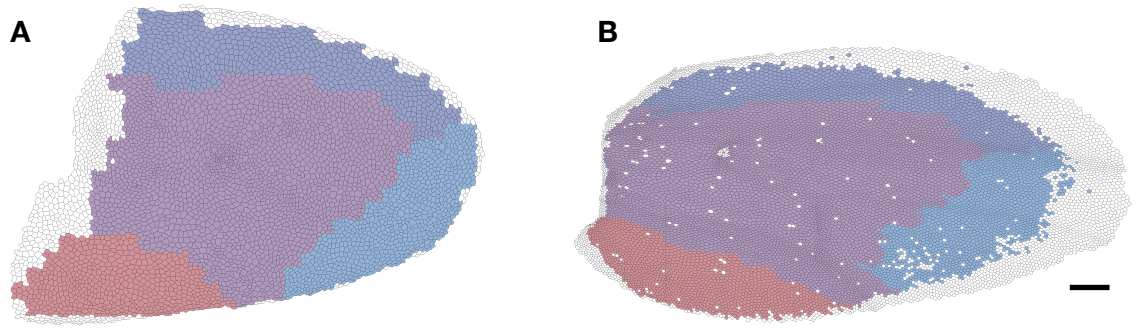

Fig. S5: Projection of the segmentation onto the wing blade cells. The segmentations based on time evolution of cellular processes were projected. (**A**, **B**) The segmentation was projected onto the wing blade cells at 15 hr (**A**) and 32 hr APF (**B**), where the regions were indicated by colors. Scale bars indicate 50 μm.

1 Pseudo codes for tissue segmentation algorithms

In below pseudo codes show algorithms of the automatic tissue segmentation. Matlab custom functions and framework developed for this study are available at GitHub (http://doi.org/10.5281/zenodo.3626111). For details of the functions and framework, see its README file and comments in the codes.

1.1 Region growing algorithm

Algorithm 1 shows a pseudo code of the region growing image segmentation in Matlab-like syntax. It divides a bitmap image stored in a data object *dataMap*. In the algorithm, a number of regions, a limit to update the seeds, and a metric are given as parameters. With the parameters, supporting objects *seedList*, *meanList*, *regionsList*, *meter*, and *seeder* are allocated and initialized. The seedList, meanList, and regionsList are instances of data object with a property *var* representing seeds and means of regions and regions, shared among the supporting objects. The meter is an object measuring distance between the mean of region and a point adjacent to the region. A method *measure* returns the distance measured by the given metric. The seeder is an object choosing seeds of regions. Methods *initalSeeds* and *initialMeans* return indices of randomly chosen points and their values. Once the dataMap was divided into regions, methods *newSeeds* and *newMeans* return indices of points at center of the regions and mean values of the regions. A method *initalQueue* returns an array where its element represents a point adjacent to one of the seeds and holds the region and distance to the region's mean value. Inside a loop, a point in the queue with the smallest distance to the region's mean value is added to the region, and points adjacent to the point, returned by a method *neighborsOfPoint* of dataMap, are added to the queue.

In our tissue segmentation, a Matlab custom function *run_region_growing*() iterates this algorithm for given time, returning a stack of resultant partitions.

1.2 Label propagation on a consensus matrix

Algorithm 2 shows a pseudo code of the label propagation. It divides N objects into clusters based on an $N \times N$ consensus matrix M whose rows and columns correspond to the objects, and an element m_{ij} represents frequency the i-th and j-th objects were included in a cluster among given clustering results. A parameter t_M indicates a threshold value, where elements in M smaller than t_M is ignored in the label propagation.

In the tissue segmentation, 50 results of region growing were converted to the consensus matrix and given to a Matlab custom function *run_label_propagation*() implementing the label propagation. Number of resultant regions is influenced by t_M, and thus a Matlab custom function *run_cm_thresholding_lp*() screens t_M value so that run_label_propagation() returns the same number of regions with the given partitions.

Algorithm 1: Region growing algorithm

```
input  : dataMap to be segmented and parameters.
% seedList, meanList, regionsList, allocatedList, meter, and seeder are
  supporting objects and variable initialized with the parameters.
seedList.var = seeder.initalSeeds;
meanList.var = seeder.initalMeans;
while loop counter is smaller than limit do
    % Initialize partition, allocated list, queue.
    regionsList.var(:) = false;
    allocatedList(:) = false;
    queue = seeder.initalQueue;
    while queue is not empty do
        point = queue(1);
        if allocatedList.var(point.index) == false then
            % Grow region to the point.
            regionsList.var(point.index, point.region) = true;
            allocatedList(point.index) = true;
            % Enqueue neighbors of the point.
            array = dataMap.neighborsOfPoint(point.index);
            for neighbor in array do
                neighbor.region = point.region;
                neighbor.distance = meter.measure(neighbor);
                queue = cat(1, queue, neighbor);
            % Remove the allocated point from queue.
            queue(1) = [];
            % Sort queue.
            [values, indices] = sort([queue.distance]);
            queue = queue(indices);
        else
            queue(1) = [];
    % Check convergnence.
    lastMeanList = meanList.var;
    seedList.var = seeder.newSeeds;
    meanList.var = seeder.newMeans;
    if isequal(lastMeanList, meanList.var) then
        break;
return regionsList.var
```

Algorithm 2: Label propagation

input : Matrix M and threshold t_M.

```
% Cut elements in M smaller than the t_M.
M(M < t_M) = 0;
% Make labelArray representing labels on N vertices.
labelArray = (1:N)';

flag = true;
while flag do
    flag = false;
    % Enumerate vertices in random order and update their label.
    for i = randperm(N) do
        % Make labelMatrix representing labels on vertices.
        labelMatrix = labelArray == 1:N;
        % Choose label most weighted by edges incident to the i-th vertex.
        ,indices= max(sum(M(:,i) .* labelMatrix),1));
        if labels(i) = indices(1) then
            % Update label of the i-th vertex.
            labelArray(i) = indices(1);
            flag = true;

% Convert labelArray to a matrix.
labelMatrix = labelArray == 1:N;
indices = any(labelMatrix,1);
partition = labelMatrix(:,indices);

return partition
```

1.3 Cellular Potts model

Algorithm 3 shows a pseudo code of the cellular Potts model. It simulates a deformation of regions (partition of dataMap) by giving small fluctuations. In the algorithm, an array of function handles, coefficients to combine the functions results, the system temperature, and number of label updates are given as parameters. With the regions and parameters, supporting objects *analyser* and *dict* are allocated and initialized. The functions in the array calculate system energy with the analyser and dict. For each fluctuation, one of points at regions rim returned by analyser *rim_points* is selected randomly, and a label of neighboring points is also selected randomly and copied. Connectedness of a region is checked locally, with a coordinate of neighboring points returned by dataMap *coordinates*.

In the tissue segmentation, a Matlab custom function *run_CPM_smoothing*() implement this algorithm with energy functions consist of area constraint, surface tension, and total silhouette value. The coefficients and temperature influence resultant regions, ans thus a Matlab custom function *run_CPM_fitting*() screens the parameters so that run_CPM_smoothin() returns smoothed regions with a circularity larger than given value and the total silhouette value as large as possible.

Algorithm 3: Cellular Potts model with region homogeneity

```
input  : Partition, dataMap, and parameters
% regionList, analyser, dict, H_functions, coefficients, T, and counter are
  supporting objects and variables initialized with the parameters.

% Calculate the system energy.
H = 0;
for k = 1:length(H_functions) do
    fh = H_functionsk;
    H = H + fh(analyser,dict) * coefficients(k);

% Update labels for given times.
while true do
    % Select a point randomly.
    rim = analyser.rim_points;
    rim = find(rim);
    if isempty(rim) then
        % There is only one region.
        break;
    i = ceil(rand() * length(rim));
    i = rim(i);

    % Select a label from neighbors of the point.
    neighbors = dataMap.neighborsOfPoint(i);
    j = ceil(rand() * length(neighbors));
    j = neighbors(j);
    if any(regionsList.var(i,:) & regionsList.var(j,:)) then
        % The i-th and j-th points are in a region.
        continue;

    % Check connectedness.
    m = zeros(3,'logical');
    x0 = dataMap.coordinates(i).x - 2;
    y0 = dataMap.coordinates(i).y - 2;
    for k = neighbors do
        x = dataMap.coordinates(k).x - x0;
        y = dataMap.coordinates(k).y - y0;
        m(y,x) = any(regionsList.var(i,:) & regionsList.var(k,:));
    array = m([1,2,3,6,9,8,7,4]);
    brray = m([2,3,6,9,8,7,4,1]);
    if sum(array ~= brray) > 2 then
        continue;

    % Get a change of energy.
    oldLabel = regionsList.var(i,:);
```

```
    regionsList.var(i,:) = regionsList.var(j,:);
    newH = 0;
     k = 1:length(H_functions)
        fh = H_functionsk;
        newH = newH + fh(analyser,dict) * coefficients(k);
    dH = newH - H;
    % Adapt the change when possible.
    p = exp(-dH / T);
    if p > rand() then
        H = newH;
        counter = counter - 1;
        if counter < 1 then
            break;
    else
        regionsList.var(i,:) = oldLabel;
return regionsList.var
```